Surfaces and Interfaces 21 (2020) 100675

Contents lists available at ScienceDirect

Surfaces and Interfaces

journal homepage: www.elsevier.com/locate/surfin

Enhanced photoelectrocatalytic performance of ZnO films doped with N_2 by a facile electrochemical method

Roberta Y.N. Reis[a], Aline. E.B. Lima[b], Maria J.S. Costa[a], João F. Cruz-Filho[a], João P.C. Moura[b], Reginaldo S. Santos[a], Geraldo E. Luz Jr[a,*]

[a] PPGQ-GERATEC-DQ-Universidade Estadual do Piauí, Rua: João Cabral, N. 2231, P.O. Box 381, 64002-150, Teresina, PI, Brazil
[b] Universidade Federal do Piauí, Departamento de Química, Teresina, PI CEP – 64049550, Brazil

ARTICLE INFO

Keywords:
N-doped ZnO films
electrodeposition
photoelectric properties
photocatalyst
advanced oxidation processes

ABSTRACT

In the present study, we investigated the structural, morphological, photoelectrochemical, and photocatalytic properties of zinc oxide (ZnO) and ZnO films, which were prepared in the presence of nitrogen (N_2) on fluorine-doped tin oxide (FTO)-conducting glass by electrodeposition and N_2 bubbling for the doped films (Zn:N). The time, N_2 flow, and calcination temperature conditions were investigated. X-ray diffraction (XRD) patterns show that ZnO and ZnO:N films have a wurtzite structure. X-ray photoelectron spectroscopy (XPS) analysis confirms nitrogen doped ZnO by both the interstitial and substitutional manners. Values at 3.25–3.27 eV of band gap energy of the films were estimated by the Tauc method. Field Emission Scanning Electron Microscopy (FE-SEM) images illustrated a change in the morphology of the ZnO:N film in relation to the ZnO film. Photoelectrochemical studies demonstrated a better photocurrent density for pure ZnO and ZnO:N films using a 20 $cm^3\ min^{-1}$ flow rate treated at 500°C with ca. 48 and 70 μA cm^{-2} (0.7 V vs. Ag/AgCl), respectively. ZnO and ZnO:N electrodes (20 $cm^3\ min^{-1}$) were used to degrade an aqueous 0.48 mg L^{-1} Rhodamine B (RhB) dye aqueous solution under polychromatic irradiation for 165 min. The degradation study was investigated under heterogeneous photocatalysis (HP) and electrochemically assisted HP (EHP) photocatalysis conditions. For RhB dye photodegradation, the performances obtained were 19% and 36% in HP for ZnO and ZnO:N, respectively. For the EHP configuration with a +0.7 V bias vs Ag/AgCl, the values were 26% and 43% for ZnO and ZnO:N, respectively. The studies presented here reveal that the N-doped ZnO films are promising candidates as photoanodes for photoelectrocatalysis applications.

1. Introduction

Semiconductor oxide films have attracted considerable attention due to applications in photoelectrochemical cells (PEC) as well as electrochemically assisted photocatalytic systems [1,2]. Among the several semiconductors studied in the literature for film production, zinc oxide (ZnO) has aroused great interest due to its low toxicity, higher load carrier mobility than other semiconductors, such as TiO_2, and thermal stability in different media [3–5]. ZnO is classified as a n-type semiconductor material with a bandgap energy (E_{BG}), varying from 3.2 to 3.4 eV [6,7], and is usually described with two types of structures: cubic or hexagonal (wurtzite). The latter is more thermodynamically stable at room temperature [8]. Other types of applications for ZnO have been reported in the literature such as electrodes for the production of dye-sensitized solar cells [9], UV light-emitting diodes [10], gas detection [11], electrochemical sensor [12,13], and capacitors [14].

For photocatalytic applications, ZnO has been applied as a dispersed catalyst in solution for the remediation of emerging contaminants [15,16]. This semiconductor has high valence band potential and high oxidative power holes, with a large E_{BG} with absorption in the ultraviolet (UV) region, causing a reduction in their efficiency in applications with the use of solar spectrum as a radiation source [3]. Therefore, the formation of composites from the semiconductor oxide mixture [17,18] and the insertion of metallic or non-metallic dopants in its structure are alternative strategies to modify the semiconductor absorption region [19,20]. For ZnO, doping nitrogen has been investigated due to the similarity between the radii of N and O atoms [21]. In general, the insertion of nitrogen into the structure of ZnO generates the maximum elevation of valence band with the formation of levels related to the hybridization of the 2p N orbital with 2p O orbital, causing increased spectral response and improved

* Corresponding author.
E-mail address: geraldoeduardo@gmail.com (G.E. Luz).

https://doi.org/10.1016/j.surfin.2020.100675
Received 3 April 2020; Received in revised form 21 July 2020; Accepted 3 September 2020
Available online 08 September 2020

photocatalytic activities [22,23]. In addition, ZnO films prepared in nitrogen atmospheres have improved electronic properties [24].

The surface and morphological properties of ZnO photoelectrodes are highly dependent on the thin film preparation process [25]. N-doped ZnO films can be synthesized with different nitrogen sources such as ammonia (NH_3), urea (CH_4N_2O), and nitrogen gas (N_2) by direct synthesis or post-synthesis treatments [26,27]. In direct synthesis, the dopants are incorporated into the ZnO network during the growth process, while in post-synthesis treatments, ZnO undergoes high temperature heat treatment in N source atmosphere [28,29]. The methods investigated and employed to obtain films of this semiconductor according to the routes described above include the chemical bath deposition [30], chemical vapor deposition [31], magnetron sputtering technique [32], hydrothermal method [33], and electrodeposition [34]. However, nitrogen doped ZnO films obtained by direct electrochemical deposition have not been reported in the literature yet. Electrochemical deposition is advantageous as it allows easy control of synthesis parameters, including applied potential, current density, and precursor concentration [35–37].

Therefore, the present work investigated the obtaining of ZnO films and direct doping of ZnO with continuous N_2 flow (ZnO:N) by electrochemical synthesis at 30 minutes. We also evaluated the influence of thermal treatment and N_2 flow rate variation (10, 20, and 30 cm^3 min^{-1}) on the optical, morphological, structural, and electrochemical properties of ZnO:N films. In addition, the films were applied as photoanodes to investigate the photocatalytic degradation of Rhodamine B (RhB) dye using two configurations: heterogeneous photocatalysis (HP) and electrochemically assisted heterogeneous photocatalysis (EHP).

2. Experimental details

2.1. Electrochemical synthesis of ZnO and ZnO:N films

ZnO and ZnO:N films were deposited on a transparent conducting substrate of fluorine-doped tin oxide (FTO-glass) by electrodeposition on potentiostatic control. The substrates were cleaned in an ultrasonic bath with neutral detergent, deionized water, and isopropyl alcohol in 15 min successive steps, respectively. The films were deposited in an electrochemical cell configured with three electrodes, and the FTO glass used as working electrode. The reference electrode and counter electrode were an Ag/AgCl (in 3.0 mol L^{-1} KCl saturated aqueous solution) electrode (in Luggin capillary) and platinum wire, respectively.

Electrochemical deposition was performed by dipping the clean FTO glass in 5 mmol L^{-1} dihydrate zinc acetate ($Zn(CH_3CO_2)_2.2H_2O$; 99%, Sigma Aldrich) aqueous solution in support electrolyte (0.1 mol L^{-1} KCl; 99%, Sigma Aldrich). Zinc oxide was deposited by electrochemical method, applying a potential of -0.9 V (vs Ag/AgCl) for 30 min. The precursor solution (pH 6.8) was kept at 75°C under constant stirring with air bubbling (130 cm^3 min^{-1} flow rate) throughout the deposition process. After drying at room temperature, the films were heat treated at different temperatures (300, 400, 500, and 600°C) heated (10°C min^{-1}) for 60 min in a muffle furnace.

For the deposition of nitrogen-doped zinc oxide (ZnO:N) films, the process was carried out under conditions similar to those previously described for ZnO. However, besides air bubbling (with flow rate of 130 cm^3 min^{-1}), the synthesis was performed with nitrogen gas (N_2) bubbling with varying flows rates of 10, 20, and 30 cm^3 min^{-1}. The N-doped ZnO films were heated at 500°C at a rate of 10°C/min for 60 min in a muffle furnace, considering the photocurrent density values obtained with ZnO films. The chemical reactions occurring in the growth process of the films during the during potentiostatic control are:

$$2H_2O + O_2 + 4e^- \rightarrow 4OH^- \quad (1)$$

$$Zn(CH_3OO)_2 + 2H_2O \rightarrow Zn^{2+} + 2CH_3OOH + 2OH^- \quad (2)$$

$$Zn^{2+} + 2OH^- \rightarrow Zn(OH)_2 \quad (3)$$

$$Zn(OH)_2 \rightarrow ZnO + H_2O \quad (4)$$

$$ZnO(OH)_2 + 1/2\,N_2 \rightarrow ZnO{:}\,N + H_2O \quad (5)$$

2.2. Structural, morphological, and electronic characterization

X-ray diffraction (XRD) patterns of the ZnO and ZnO:N films were obtained using a diffractometer (Empyrean, 2, PANalytical) with Co_α radiation source (λ = 0.178901 nm) in the 2θ range of 20° to 90° with a scanning velocity of 0.02°. The diffraction patterns were compared to the data from the Inorganic Crystal Structure Database (ICSD). The morphology of the photoelectrodes was characterized by field emission–scanning electron microscopy (FE-SEM, FEI Quanta FEG 250). The images were obtained with a working voltage of 20 kV. Nitrogen doping level was analyzed by X-ray photoelectron spectroscopy (XPS) on a scienta omicron ESCA spectrometer (Germany) using a monochromatic x-ray source of Al Kα (1486.7 eV) under vacuum condition <10–8 mbar and 400 μm spot size. The survey spectral resolution was 0.5 eV with 5 scans, and higher resolution spectra were 0.05 eV with 50 scans. The binding energy (BE) of the C 1s (285 eV) was used as internal standard reference for the BE scale.

2.3. Optical characterization and photoelectrochemical measurements

Optical properties of films were measured using a Shimadzu spectrophotometer (Model UV-2600) equipped with an integrating sphere using barium sulfate as a reference standard. From the film transmittance spectra, optical band gap energy (E_{BG}) values were estimated by the TAUC method [38], assuming the following direct light transition, according to the equation [39]:

$$(\alpha h\nu)^2 = C(h\nu - E_{BG}) \quad (6)$$

where, $h\nu$ is an incident photon energy, C is a proportionality constant, E_{BG} is a forbidden band gap energy interval; thus, electron transition occurred from the valence band to the conduction band, i.e., the optical transfer coefficient of the film.

The photoelectrochemical properties were investigated in a photoelectrochemical cell (PEC) equipped with an optical glass window (100% transmittance for $\lambda >$ 360 nm). Using a three-electrode-system configuration and a 0.1 mol L^{-1} Na_2SO_4 (99%, Sigma Aldrich) aqueous solution (pH 6.6) as a support electrolyte. The working electrodes were ZnO and ZnO:N films (ca. 1 cm^2 geometric area), a Pt wire was used as a counter electrode and Ag/AgCl as reference electrode (in a Luggin capillary). Measurements were performed with a Galvanostat/potentiostat (autolab PGSTAT 302-N Metrohm) and NOVA 1.7 software in the absence of light (dark) and under polychromatic irradiation. A metal vapor discharge lamp (HQI-TS NDL) with a nominal potency of 150 W was employed to irradiate the samples. Photocurrent density was measured by cyclic voltammetry (CV) with a scan rate of 20 mV s^{-1} in the dark and under polychromatic irradiation. Flat band potential (E_{fb}) was determined from the Burtler-Gärtner model based on linear scanning voltammetry (LSV) [40], with data recorded in the anodic potential range from 0.1 to 1.2 V at a scan rate of 1.0 mV s^{-1}, using chopped illumination (manual chopper) at 0.1 Hz. The variation in photocurrent generated by the ZnO and N doped ZnO electrodes was measured by the chronoamperometry curves in dark and light conditions polarized with potential at +0.7 V (vs. Ag/AgCl).

For comparison, the potential recorded with the Ag/AgCl reference electrode was adjusted to a reversible hydrogen electrode (RHE) according to the equation [41]:

$$E(\text{vs. RHE}) = E(\text{vs. Ag/AgCl}) + 0.0591\,V \times pH + 0.199V \quad (7)$$

In addition, the potentials after adjustment for RHE (in volts) were converted to electron volts (eV) using the equation [42]:

$$E(eV) = [-4.5\,eV - eE\,(RHE)] \quad (8)$$

2.4. Rhodamine B dye degradation studies

The photocatalytic activity of ZnO and ZnO:N (20 cm^3 min^{-1}) electrode photocatalysts was investigated using a RhB dye aqueous solution (95%, Sigma – Aldrich) with an initial concentration (C_0) of 1.0 μmol L^{-1} dissolved in 0.1 mol L^{-1} Na_2SO_4 aqueous solution as a supporting electrolyte (pH 6.6). In this investigation, three configurations were considered: (i) photolysis by irradiation of 15 mL RhB dye in the supporting electrolyte without the photocatalyst film employing only a clean FTO-glass; (ii) heterogeneous photocatalysis (HP) using only a photocatalyst film system; and (iii) electrochemically assisted heterogeneous photocatalysis (EHP) in a three-electrode-system configuration, which was performed with polarized photoelectrodes at + 0.7 V vs Ag/AgCl. In all configurations, the system was illuminated by polychromatic irradiation (metal vapor discharge lamp, 150 W) without heat or agitation. The kinetic investigation occurred under darkness and irradiated conditions for 2 h and 45 min; thus, aliquots were collected at different time intervals and analyzed using the UV-vis spectrophotometer. The degradation efficiency (η) was calculated according to the following equation: $\eta = \frac{A_0 - A_t}{A_0} x100$, where A_0 is the initial absorbance, and A_t is the absorbance of RhB dye after the irradiation time "t ".

3. Results and discussion

3.1. Structural and morphological characterization ZnO and ZnO:N films

The structural properties of heated ZnO films at 300, 400, 500, and 600°C and ZnO:N films prepared with N_2 flow rate of 10, 20, and 30 cm^3 min^{-1} and treated at 500°C were evaluated by XRD. Fig. 1 illustrates the XRD patterns for ZnO and ZnO:N films. All diffraction peaks are in good agreement with the ZnO hexagonal (wurtizite) structure (ICSD No. 65119) [43]. The diffraction peaks at 30.5°, 38.8°, 43.8°, 60.3°, 64.0°, 72.6°, 77.6°, and 82.8°, identified with asterisk (*), correspond to the crystalline phases of the FTO substrate [44]. XRD data for ZnO films in different thermal treatments (Fig. 1a) indicate the occurrence of a preferential orientation in the plane (101). An intense peak located at 32.7° refers to the presence of zinc hydroxide ($Zn(OH)_2$, ICSD No. 36229) [45]. $Zn(OH)_2$ is intermediate chemical compound in the reaction of ZnO formation by electrochemical route and increasing the temperature of calcination caused the transformation of $Zn(OH)_2$ to ZnO [46]. A reduction in the intensity of the diffraction peaks in the calcined film at 600°C indicates an interaction between the FTO substrate material and the formed ZnO film.

From the electrochemical studies of ZnO films (Fig. 5), the film at 500°C presented the best photocurrent density value; thus, the thermal treatment studies to synthesize ZnO:N films were performed at 500°C. In the ZnO:N films (10, 20, and 30 cm^3 min^{-1}) (Fig. 1b), XRD patterns are in agreement with the ZnO wurtzite structure (ICSD No. 65119). The intense peak at 33°, similar to that observed for ZnO, is due to Zn $(OH)_2$ (ICSD No. 36229), which may indicate that the nitrogen-rich medium makes it difficult to dehydrate Zn $(OH)_2$ to form ZnO. All XRD peaks of ZnO:N films present displacement to higher angles as shown in Fig. 1c. The occurrence of displacements may be related to the formation of Zn-N bonds in the ZnO network due to the similarity of the atomic rays of oxygen and nitrogen [47]. A reduction in peak intensities occurred when compared to pure ZnO at 600°C.

ZnO and ZnO:N films synthesized by electrochemical route on conducting surface (FTO-glass) with a 1 cm^2 geometric area and calcined at 500°C had an immobilized particle density of ca. 1.9 and 2.1 mg cm^{-2}, respectively. Fig. 2 is FE-SEM images of the surface of ZnO and ZnO:N and the cross section of ZnO film prepared in the presence of N_2 deposited on FTO-glass. The FE-SEM image of the calcined ZnO film at 500°C (Fig. 2a) exhibits the formation of a compact layer of agglomerated particles with undefined shapes and irregular edges. A

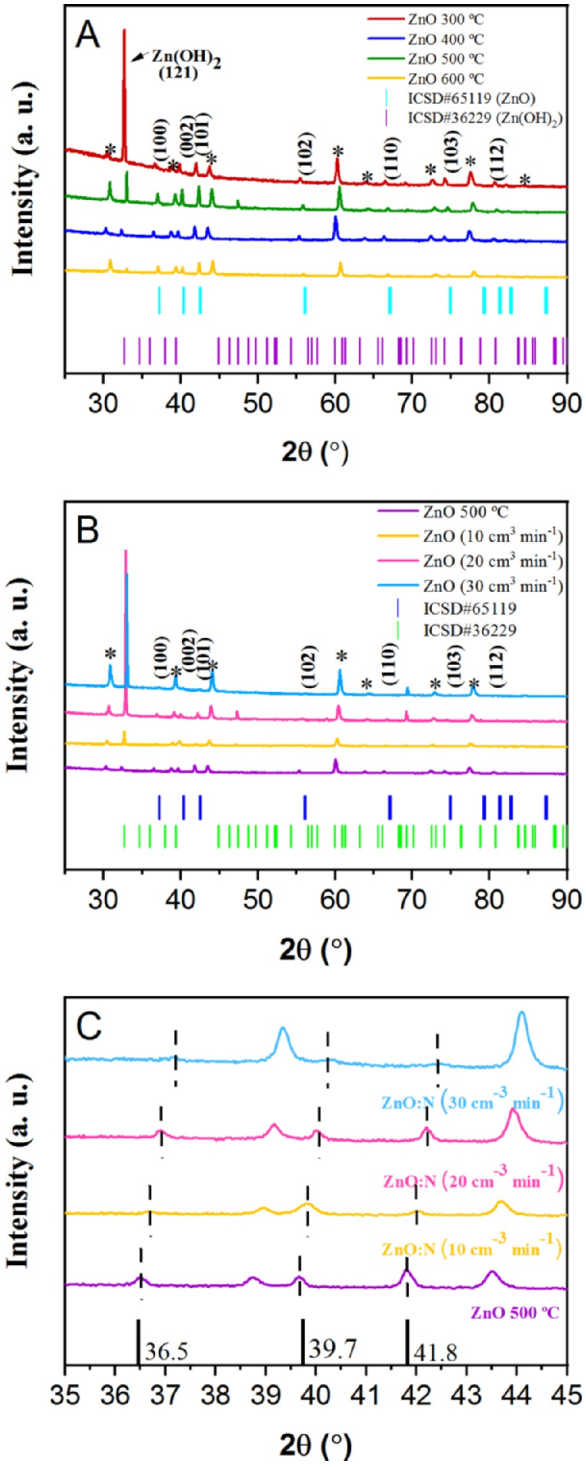

Fig. 1. XRD patterns of (a) ZnO films annealed at 300, 400, 500, and 600°C; (b) ZnO:N (10, 20, and 30 cm^3 min^{-1}) films calcined at 500°C; and (c) enlarged view of the three diffraction peaks and vertical lines of ZnO data (ICSD No. 65119). Vertical bars indicating the position of the hexagonal ZnO and Zn $(OH)_2$ planes.

modification in the morphology of ZnO films was observed after prepared in the presence of N_2, with particle formation in the form of agglomerated thin discs (Fig. 1(b) insert) with regular edges and average diameter of 0.33 ± 0.03 μm irregularly distributed on the substrate. Singh et al. [48] reported that films synthesized under nitrogen flow atmosphere facilitate the formation of spherical ZnO:N clusters and contribute to non-uniform film growth. The cross section of

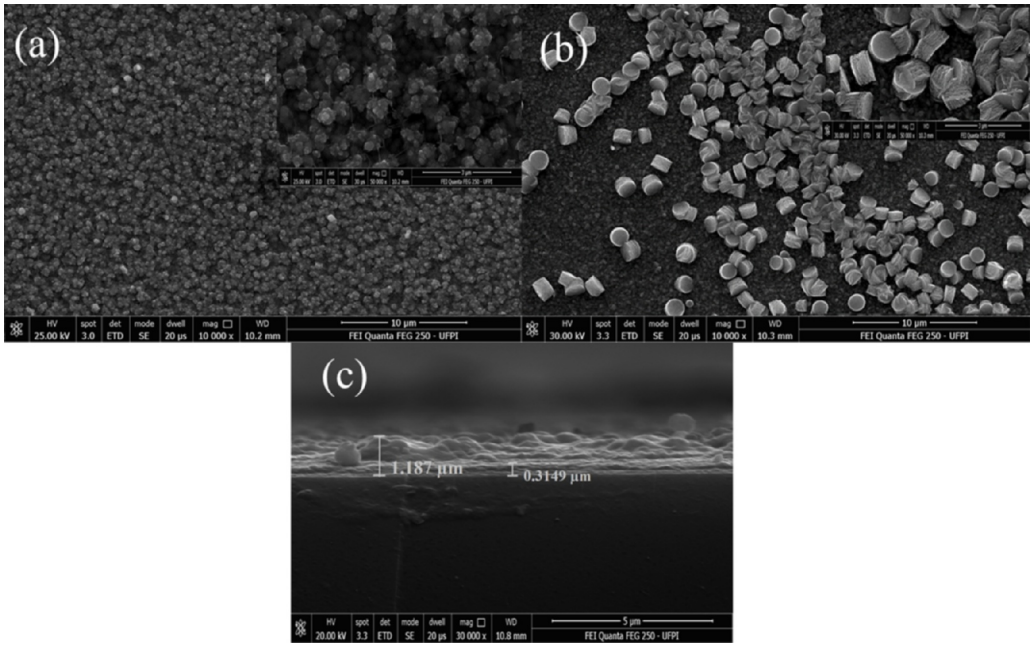

Fig. 2. FE-SEM images of (a) ZnO films annealed at 500°C; (b) ZnO: N films annealed at 500°C; and (c) cross-section FE-SEM images of ZnO: N films.

ZnO film prepared in the presence of N_2 is illustrated in Fig. 2 (c) and reveals that the average thickness is 1.19 ± 0.01 µm.

To confirm the incorporation of nitrogen in the structure of the ZnO films synthesized in the presence of N_2, X-ray photoelectron spectroscopy (XPS) analyzes were performed for the ZnO and ZnO:N films (10, 20, and 30 cm^3 min^{-1}) treated at 500°C. The XPS spectra of the ZnO and ZnO:N films over a wide energy range are presented in Fig. 3. The similar survey spectra (Fig. 3 (a)) for the ZnO and ZnO:N films (10, 20, and 30 cm^3 min^{-1}) indicate that the principal elements are zinc (Zn) and oxygen (O). For ZnO:N films, a small signal related to nitrogen can be observed, indicating the presence of N in this films. The presence of the carbon peak (C 1s) at 285 eV in all samples could be due to carbon dioxide adsorption on samples surface and some residues from synthesis method.

For better analysis of the elements, high resolution spectra for Zn 2p, O 1s, and N 1s were scanned and are shown in Fig. 3 (b)–(d), respectively. Energy peaks characteristic of ZnO are observed in Zn 2p core level spectra (Fig. 3 (b)) for all samples in 1020.1–1020.4 eV (Zn $2p_{3/2}$) and 1043.2–1043.5 eV (Zn $2p_{1/2}$) [49]. A shift in the binding energy for the films synthesized with a variation of nitrogen flow indicates that the presence of N interferes with the Zn-O binding. Therefore, deviations in the central lines of Zn $2p_{3/2}$ and $2p_{1/2}$ indicate

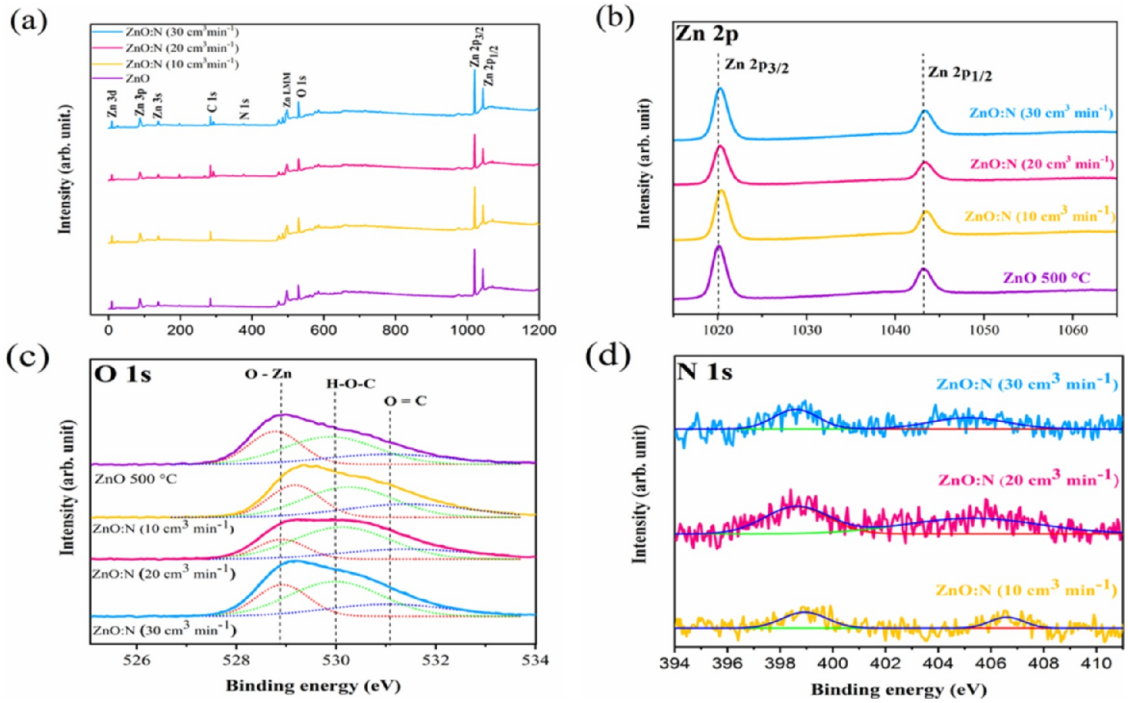

Fig. 3. XPS spectra of (a) Survey spectra ZnO and ZnO:N films (10, 20, 30 cm^3 min^{-1}) at 500 °C, (b) Zn 2p high resolution spectra, (c) O 1s high resolution spectra and (d) N 1s high resolution spectra ZnO: N films (10, 20, 30 cm^3 min^{-1}).

the N doping process, with possible formation of Zn-N bond [50].

Fig. 3 (c) contains the core level spectra O 1s for the ZnO and Zn:N films fitted by Gaussian deconvolution. The displacements in binding energies O 1s spectra of ZnO:N films can indicate a change in the ZnO film network after the doping process. Three energy peaks are observed. The peak energy deconvolved at 528.9–529.2 eV corresponds to the Zn-O binding energy characteristic of the ZnO hexagonal (wurtzite) structure [51]. The peak at 530.0–530.4 eV is indicative of oxygen vacancies (V_o) in the ZnO structure, and the peak at 531.1–531.6 eV is related to the C=O binding energy referring to carbon dioxide adsorbed on the surface of the films [52]. The deconvolved spectra O 1s demonstrated that nitrogen doping increased ZnO oxygen vacancies, which can indicate a substitutional doped.

Fig. 3 (d) illustrates the high-resolution XPS spectra in the N 1s region for ZnO:N films fitted by Gaussian deconvolution. The presence of two peaks prove the doping of the films synthesized with N_2 fluxes in the rates of 10, 20, and 30 $cm^3\ min^{-1}$, corroborating the observed XRD displacements. A peak in the region at 398.6–398.9 eV referring to substitutional doping with the incorporation of nitrogen in the structure of the ZnO film (O-Zn-N). The other peak is observed at 405.1–406.6 eV, showing that interstitial doping of nitrogen also occurs in the ZnO films [23,53]. The interstitial and substitutional dopings have a different influence on photocatalytic activity and the properties of the semiconductor [50,54]. The existence of interstitial doping for ZnO films after the doping process with different rate of N_2 implies its maintenance as an *n*-type semiconductor, contributing to a better photocatalytic efficiency [55]. The substitutional doping induces oxygen vacancies, as beforehand indicated in the O 1s spectra, which can improve the photoelectrochemical and photocatalytic properties of the ZnO:N films [50].

3.2. Optical and photoelectrochemical properties of ZnO and ZnO:N films

Optical E_{BG} values were estimated for ZnO and ZnO:N films using the Tauc method, assuming direct electron transitions values [56]. E_{BG} values were calculated from the $(\alpha h\upsilon)^2$ versus $h\upsilon$ graph, and the linear portion of the graph was extrapolated to $(\alpha h\upsilon)^2$ equal to zero, intersecting the energy axis as shown in Fig. 4. The forbidden band gap energy values for ZnO films at 300, 400, 500, and 600°C (Fig. 4 (a)) were 3.26, 3.28, 3.25, and 3.26 eV, respectively. Therefore, the values obtained for the films are in good agreement with the literature [5,36]. For films prepared with N_2 at 10, 20, and 30 $cm^3\ min^{-1}$ (Fig. 4 (b)), the E_{BG} value was estimated in 3.26 eV and 3.27 eV, respectively. E_{BG} values indicate that the doping process with N did not cause modification of the prohibited band gap energy value as presented in previous works [52,57]. The intermediate energy levels formed between the conduction band (CB) and valence bands (VB) did not significantly alter the forbidden band energy values, as reported in literature [58]. This behavior can be related to both interstitial and substitutional N-doped ZnO evidenced by XPS results. According to Meng et al. [59] and Silva et al. [50], the two types of doping processes result in a contradictory effect in ZnO band gap energy.

The photoelectrochemical properties of ZnO and ZnO:N films were investigated using a three-electrode setup in 0.1 mol L^{-1} aqueous Na_2SO_4 solutions. Fig. 5 displays the photocurrent densities for ZnO (300 to 600°C) and ZnO:N (10, 20, and 30 $cm^3\ min^{-1}$) electrodes recorded using cyclic voltammograms in the dark with polychromatic irradiation (20 mVs^{-1}). Voltammetry measurements elucidated that the electrodes exhibited positive photocurrent values as expected for n-type semiconductor electrodes at higher potentials. In this condition, the holes move to the electrode surface and oxidize the species in solution, producing an anodic photocurrent [60].

Cyclic voltammetry curves for electrodes in dark conditions displayed an almost zero capacitive current. In potentials greater than 1.0 V (vs. Ag/AgCl), low photocurrent values (0.68 μA cm^{-2}) associated with the oxygen evolution reaction (OER) were observed (Fig. 5). This potential value serves to limit the potential window in anodic direction. To investigate the influence of calcination temperature on the photoelectrochemical response of ZnO films, ZnO electrodes were heated at 300, 400, 500, and 600°C; and the results are presented in Fig. 5 (a). Under polychromatic irradiation, the increase of the calcination temperature favored the increase of photocurrent density of the films. The calcined ZnO electrodes at 300, 400, and 500°C achieved photocurrents of ca. 30, 40, and 48 μA cm^{-2} at 0.7 V (*vs.* Ag/AgCl), respectively. This behavior can be attributed to better crystallinity demonstrated in XRD analysis. The increase in crystallinity facilitates the development of the depletion region, which generates the electric field that separates the carriers of photogenerated charges through electron transport. The oxidation reactions through holes in the semiconductor surface are favored and the recombination centers decrease [61]. Oliveira et al.[62] reported better photocatalytic activity for nitrogen-doped ZnO on Rhodamine B dye degradation due to better crystallinity provided by doping and heat treatment at 500°C. However, calcined at 600°C showed a lower photocurrent density of ca. 15 μA cm^{-2} at 0.7 V (vs. Ag/AgCl), which can be explained by the sintering of the deposited material and the components present on the FTO glass, demonstrated by a lower intensity of XRD peaks. As the ZnO electrode at 500 °C presented the best photocurrent density value, all subsequent photoelectrochemical studies were performed in ZnO electrodes synthetized in the presence of N_2 by thermal treated at 500°C.

Fig. 5 (b) contains the cyclic voltammograms for ZnO films prepared with N_2 at 10, 20, and 30 $cm^3\ min^{-1}$ compared to pure ZnO. To analyze the effects of the amount of N_2 added to the ZnO structure, the N_2 flow rate during the synthesis process was varied. The films with flow rate of

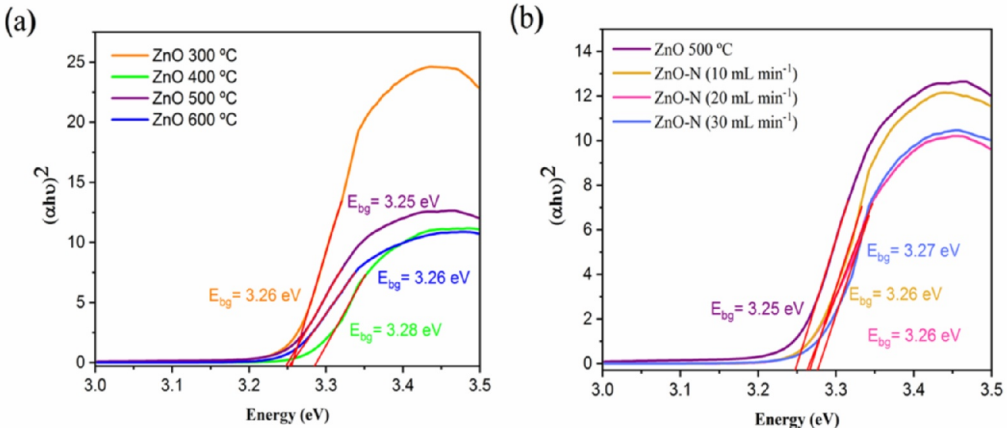

Fig. 4. Plot of $(\alpha h\nu)^2$ versus energy for (a) ZnO films annealed from 300°C to 600°C and (b) ZnO: N films (10, 20, and 30 $cm^3\ min^{-1}$) annealed at 500°C.

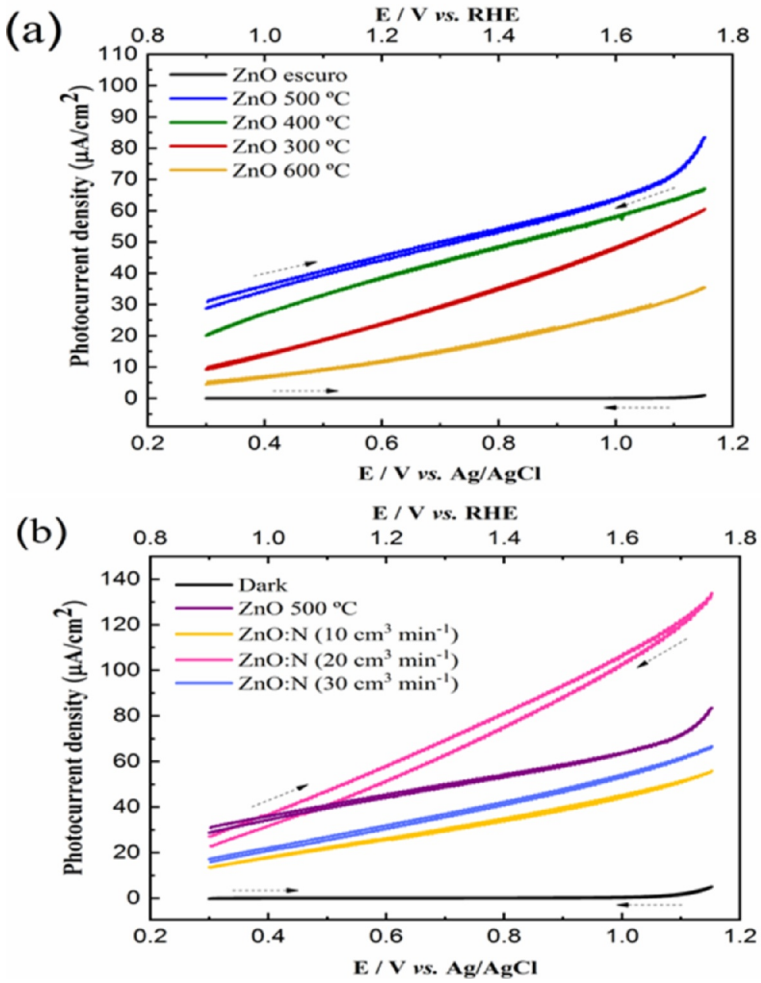

Fig. 5. Cyclic voltammetry curves with 20 mV s^{-1} scan rate in Na_2SO_4 aqueous solution (0.1 mol L^{-1}) in the dark and under polychromatic irradiation for the (a) ZnO electrodes at different temperatures (300 to 600°C) and (b) ZnO: N electrodes with flow rate of 10, 20, and 30 cm^3 min^{-1} annealed at 500°C.

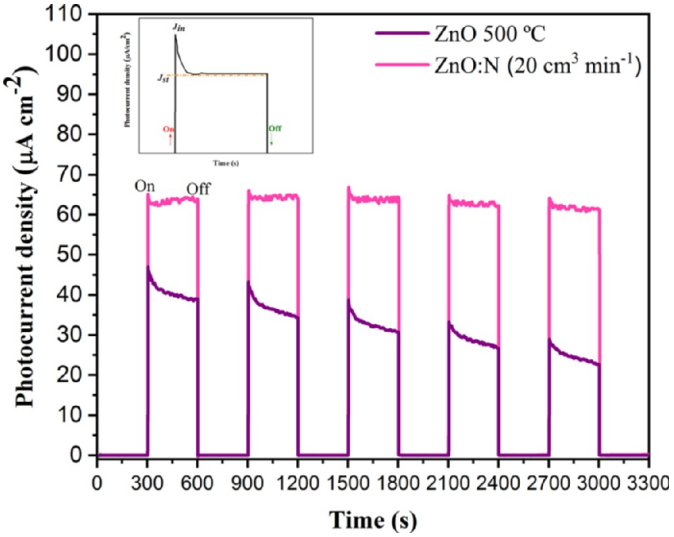

Fig. 6. Comparison of transient photocurrent for ZnO and ZnO: N films (20 cm^3 min^{-1}) at 500°C from the chronoamperometry curves under 300 s chopper polychromatic irradiation at 0.7 V (vs Ag / AgCl). Insert: representation of J_{in} and J_{st} values after polychromatic irradiation.

10, 20, and 30 cm^3 min^{-1} presented photocurrent values of ca. 30, 70, and 37 μA cm^{-2} at 0.7 V (vs. Ag/AgCl), respectively. The increase of N_2 flow rate from 10 to 20 cm^3 min^{-1} favored the increase of photocurrent density. ZnO:N electrode with flow rate of 20 cm^3 min^{-1} exhibited better photocurrent density value; this result suggests that N doped films present greater electron mobility, as well as lower electrical resistance and, consequently, a better efficiency in the transportation of photogenerated charges. Thus, the preparation of improved ZnO:N film, discussed by XRD and XPS analysis, was confirmed by photoelectrochemical studies. Although no significant variation in the optical values of E_{BG} was recorded after synthesis in the presence of N_2, the XRD, XPS, and photoelectrochemical analyses confirm the electronic changes in the ZnO materials [63,64]. Allami et al. [65] reported that the improved photoelectrochemical performance of ZnO films synthesized in nitrogen atmosphere as electrode can be attributed to greater mobility of the majority charge carriers and a reduction in electron/hole (e^-/h^+) pair recombination. The photocurrent reduction for the film prepared in 30 cm^3 min^{-1} flow rate may be related to defect formation and increased recombination rate of the photogenerated e^-/h^+ pairs [66]. From the results obtained with N_2 flow variation, further studies were performed with ZnO: N films prepared at 20 cm^3 min^{-1}.

The photoelectrochemical properties and photocatalytic activity of ZnO films depend on the recombination rate and ZnO photostability under long irradiation time [67]. Besides contributing to a better performance in visible radiation, nitrogen-doping is also an alternative to improve the chemical stability of ZnO and reduce the recombination rate of photogenerated pairs, favoring better photocatalytic

performance, as previously reported [68]. Fig. 6 displays the photocurrent density responses of the ZnO and ZnO:N (20 cm^3 min^{-1}) films, evaluated by 0.7 V (1.23 V *vs* RHE) constant bias potential chronoamperometry curves with 300 s manual-chopped.

The initial anodic photocurrent (J_{in}) peak in Fig. 6 indicates the injection of electrons caused by the charge separation process, that is, the formation of the e^-/h^+ pairs. As previously reported, considering the theory discussed for reactions at the electrolyte/n-type semiconductor electrode interface, after irradiation, the holes move toward the semiconductor surface, where they are reduced by species in the electrolyte, and electrons move for the conductive substrate to be collected by the external circuit. Fig. 6 illustrates that the photocurrent decreases over time until it reaches a stable photocurrent density, J_{st}, indicating the occurrence of the charge recombination process. According to studies by Costa et al. [69], this current decay process is independent of the established mass transport process and attributed only to the charge recombination processes. By disrupting the light, the CB electrons return to VB resulting in an almost zero photocurrent [70]. The photocurrent responses of the films in the chronoamperometry curves agree with the cyclic voltammetry results, displaying a higher photocurrent density for the ZnO: N films (20 cm^3 min^{-1}), which is ca. 1.4 times higher than pure ZnO. In addition, a better stability in photocurrent densities occurred with the irradiation time for the nitrogen doped electrodes.

The initial photocurrent density (J_{in}) and stationary photocurrent density (J_{st}) results for the ZnO electrode depict the existence of e^-/h^+ pair recombination. This was demonstrated by Spadavecchia et al. [71], who, in their studies of transient photocurrent with TiO_2 electrodes, determined the lifetime for the charge recombination processes in the films (τ) from the chronoamperometric curves by the relationship between J_{in} and J_{st} with J_t (photocurrent density at time "t"). However, for the ZnO:N electrodes (20 cm^3 min^{-1}), the chronoamperometric curves present similar J_{in} and J_{st} values, distancing themselves from the behavior presented in Fig. 6 and suggesting that the recombination processes for the film after synthesizing with N_2 is minimal.

To prove the stability of the ZnO film prepared in the presence of N_2 under polychromatic irradiation for an extensive time, a chronoamperometric study was performed maintaining the irradiated film for 4 h without interruption (Fig. 7). The ZnO film prepared with a flow rate of 20 cm^3 min^{-1} presented good stability during this irradiation time, corroborating with the study reported in Fig. 6. Thus, the process

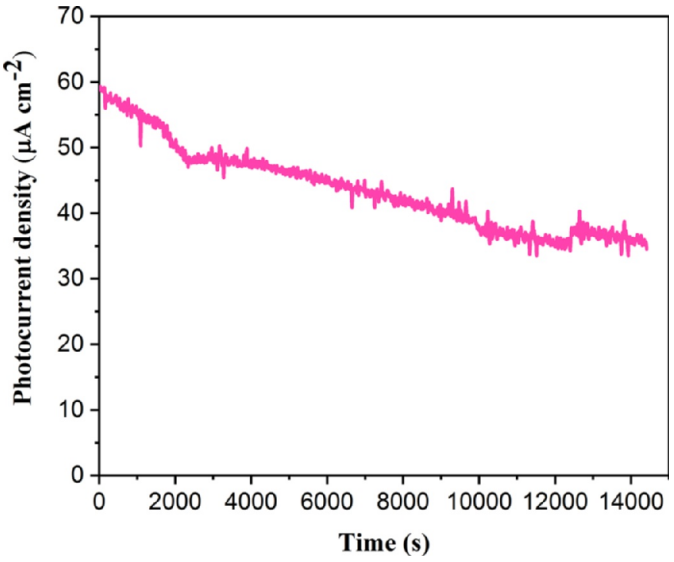

Fig. 7. Stability test for ZnO: N (20 cm^3 min^{-1}) electrode at 500°C under 4h without interruption of light in 0.1 mol L^{-1} Na_2SO_4 aqueous solution with constant potential of 0.7 (V *vs.* Ag/AgCl).

of film synthesis in N_2 atmospheres is influenced by the amount of dopant and may help to increase recombination lifetime by creating electronic levels in the forbidden band gap interval that selectively captures charge carriers [72,73].

Linear scan voltammetry (LSV) results for pure ZnO and ZnO:N (20 cm^3 min^{-1}) electrodes calcined at 500°C using a 10 s manual chopper irradiation interval are provided in Fig. 8 (a) and (b). As discussed earlier, the N-doping process contributed to a better photocurrent density result for the ZnO electrode. From the LSV curves the flat band potential ("flat band", E_{fb}) was determined for the films (Fig. 8 (a) and (b) insert). E_{fb} is considered an approximation of the Fermi level potential and expresses for n-type semiconductor the electron reducing power in CB, making it possible to estimate its application in any photoelectrochemical proposition. Its value can be determined by applying the Burter-Gärtner model [41]. E_{fb} values for pure ZnO and ZnO:N films were determined using the Burter-Gärtner model, according to the methodology adopted by Lima et al. [74]. The E_{fb} values (Fig. 8 (a,b)) determined for the ZnO and ZnO:N (20 cm^3 min-1) electrodes are -0.06 V (0.53 V *vs.* RHE) and 0.11V (0.70 V *vs.* RHE), respectively. The variation in E_{fb} values and the profile change in the linear voltammetry curves after the preparation of films in N_2 atmospheres verify the incorporation of nitrogen into the ZnO structure, corroborating the previously reported XRD, FE-SEM, XPS, and voltammetry results [75].

Fig. 8 (d) represents the relative positions of the ZnO and ZnO:N conduction and valence bands edges, estimated on the vacuum energy scale relative to the RHE using Eq. 2 and Eq. 3. The data junction E_{fb} and E_{BG} generated the band position diagram for the electrodes. The CB edge value was estimated using E_{fb}, and the VB edge was calculated from the difference between CB and VB corresponding to the semiconductor forbidden band gap energy. As previously described, the exact position of the valence and conduction band edges depends on the characteristics of the semiconductor electrode and the solution [76].

To evaluate the possible application of ZnO and ZnO:N electrodes for the photocatalytic oxidation of RhB dye, an energy diagram for the semiconductor/dye interface in aqueous solution was assembled, considering the positions of VB and CB for semiconductors, highest occupied molecular orbitals (HOMO), and the lowest unoccupied molecular orbitals (LUMO) energies for the dye (Fig. 8). Fig. 8 (c) shows in dark voltammograms (20 mV s^{-1}) obtained from the solution with RhB dye in 0.1 mol L^{-1} Na_2SO_4 support electrolyte (15 mL) with a potential range of 0.3 at 1.15 V (vs. Ag/AgCl). A peak oxidation current was observed with a potential onset of 0.75 V and a maximum peak of 0.92 V for the 1.0 μmol L^{-1} Rhodamine B aqueous solution. The RhB oxidation potential obtained was converted to energy scale using Eqs. 2 and 3, resulting in -6.0 eV. For organic compounds, this maximum oxidation energy value can be attributed to the HOMO. Based on the UV-Vis absorption graph shown in the insert of Fig. 8 (c) for RhB, the forbidden band energy between the HOMO and the LUMO dye was estimated [41,70].

The RhB dye UV-Vis absorption spectrum had a maximum absorption band at 553 nm. Assuming that [E (eV) = 1241 / λ (nm)], the forbidden band gap energy value of the dye is equivalent to 2.24 eV. Thus, the energy level of the LUMO energy was determined from the oxidation potential of RhB and the estimated forbidden band gap energy value for the dye, obtaining a value of -3.76 eV. Knowing the relative positions of the band edges and the pollutant oxidation potential, allows estimation of semiconductor efficiency in photocatalytic reactions [77]. The energy diagrams for the RhB dye and the ZnO, ZnO:N electrodes are shown in Fig. 8 (d). The energy diagram for the semiconductor/dye interface implies the occurrence of RhB dye oxidation on the electrode surface under visible light irradiation, because the dye molecule HOMO is less negative than the ZnO and ZnO:N (20 cm^3 min^{-1}) VB. Thus, the photogenerated holes in the valence band are capable of oxidizing RhB. Compared with the ZnO electrode, the photoinduced charge separation should be improved for the ZnO:N

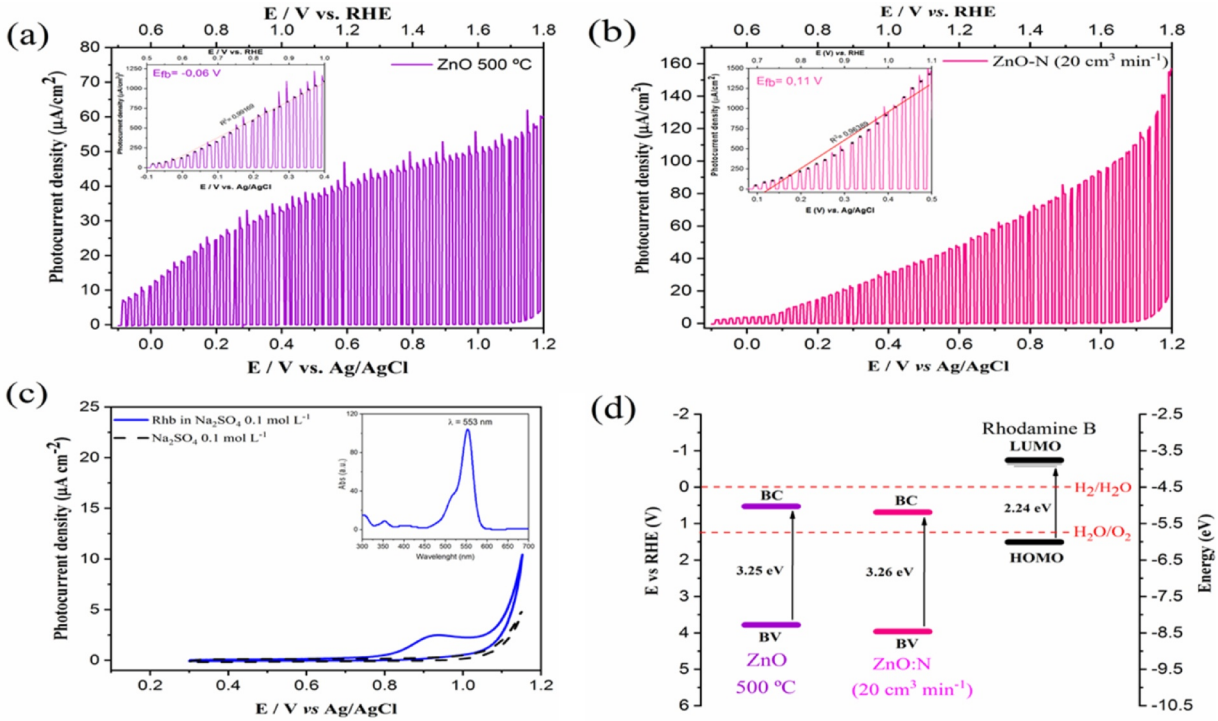

Fig. 8. Linear Scanning Voltagrams (LSV) of (a) ZnO and (b) ZnO: N (20 cm^3 min^{-1}) films at 500°C in Na_2SO_4 support electrolyte (pH 6.6) under 10 s chopper of visible light with range from -0.1 to 1.2 V (vs. Ag / AgCl) anodic potential with a scan rate of 1.0 mV s^{-1}. (c) Cyclic voltammograms (20 mV s^{-1}) of the Rhodamine B dye aqueous solution (1.0 μmol L^{-1}) in 0.1 mol L^{-1} Na_2SO_4 in the dark (Insert: Rhodamine B dye UV-vis analysis), and (d) energy diagram for photocatalyst/RhB dye interface in aqueous solution, considering the HOMO and LUMO of dye as well as the BV and BC edges of the ZnO and ZnO:N electrodes.

electrode, as nitrogen-doping increases electron transport efficiency, provides greater chemical stability under visible light, and slows down the recombination process.

3.3. Rhodamine B photodegradation

The evaluation of photocatalytic activity of ZnO and ZnO:N films (20 cm^3 min^{-1}) with ca. 1 cm^2 in the degradation of RhB dye in aqueous medium (C_0 = 1.0 μmol L^{-1}) was studied using the systems in the HP and EHP configuration under polychromatic irradiation. The results of RhB dye photodegradation are in Fig. 9. In the HP configuration, the photoanodes and the counter electrode were maintained to E = 0 V (*vs.* Ag / AgCl); and, in the EHP conditions, the irradiated semiconductor electrodes were polarized to 0.7 V (*vs.* Ag / AgCl) to minimize recombination of charges and to improve dye photoelectrochemically assist oxidation. For comparison, the degradation reaction of a RhB dye aqueous solution without catalyst (photolysis) was performed.

Fig. 9 (a) shows the photocatalytic results for the ZnO and ZnO:N (20 cm^3 min^{-1}) electrodes. Initially, the adsorption process on the catalyst surface was evaluated for a time of 30 min with no irradiation. Immediately after the irradiation process, RhB dye concentration decreased over time (SM 1a−e), related to the formation of photogenerated oxidant species in the catalytic system [78]. The degradation efficiency of photolysis before irradiated RhB dye was 15.6% after 165 min under irradiation (Table 1). For HP, photocatalysts ZnO and ZnO:N exhibited degradation efficiencies of 19.0% and 36.6%, respectively, at the same irradiation time. In the EHP configuration, the ZnO and ZnO:N photocatalysts obtained degradation efficiency values higher than those described for the HP configuration with 26.0% and 43.0%, respectively. Compared to the photolysis process, the HP and EHP configurations reached higher efficiency values, with emphasis on the processes performed in the EHP configuration.

The degradation kinetics of RhB dye is shown in Fig. 9(b). To calculate the kinetic parameters of the RhB dye photodegradation process and to investigate the influence of the process on the photocatalytic degradation rate of RhB, a pseudo-first order kinetic model derived from the Langmuir-Hinshelwood model was applied [79]. The Langmuir-Hinshelwood kinetic model is commonly used to describe the kinetics of a heterogeneous photocatalytic reaction. This model assumes that adsorption of dye molecules occurs on the catalyst surface prior to photocatalytic processes [80]. Photocatalytic rates were calculated using the equation [81], $\ln(\frac{A_t}{A_0}) = -kt$, where k is a RhB dye degradation rate constant (min^{-1}), and t is the irradiation time in minutes. Therefore, RhB dye photodegradation was adapted to a plot of ln (A_t/A_0) *vs* time to obtain the constant degradation rate. According to Table 1, the k-value for photolysis in RhB dye removal process was 6.57 × 10^{-4} min^{-1}, for ZnO electrode in HP and EHP systems were 9.69 × 10^{-4} and 1.75 × 10^{-3} min^{-1}, respectively. After N-doping, higher values were obtained for the HP and EHP configuration of 2.16 × 10^{-3} and 2.38 × 10^{-3} min^{-1}, respectively, reinforcing the better efficiency of EHP configuration in relation to HP.

The EHP configuration occurs with biased potential electrodes. In *n*-type semiconductors after irradiation, the electrons are conducted to the conducting substrate, which is collected by the counter electrode, and the holes migrate to the photoanode/electrolyte interface, contributing to the increase in the separation of charges and the reduction in recombination of the photogenerated e^-/h^+ pairs [82]. Thus, a better pollutant degradation rate can be achieved in photocatalytic tests. Ojani and Zarei [83] highlighted the efficiency of hydrazine oxidation from Ti/TiO_2 electrodes using potential at 0.8 (*vs.* Ag / AgCl) when compared to existing methods. Santos et al. [84] reported better results for the TiO_2 and Ag-TiO_2 electrodes with the EHP configuration in photocatalytic remediation of contaminated water with gram-negative and gram-positive bacteria from E. coli and S. aureus.

The better photocatalytic performance of ZnO:N electrode in relation to ZnO film, in both HP and EHP configurations, can be related to both the formation of intermediate levels in the prohibited band gap energy and the increased oxygen vacancies due to nitrogen doping, as

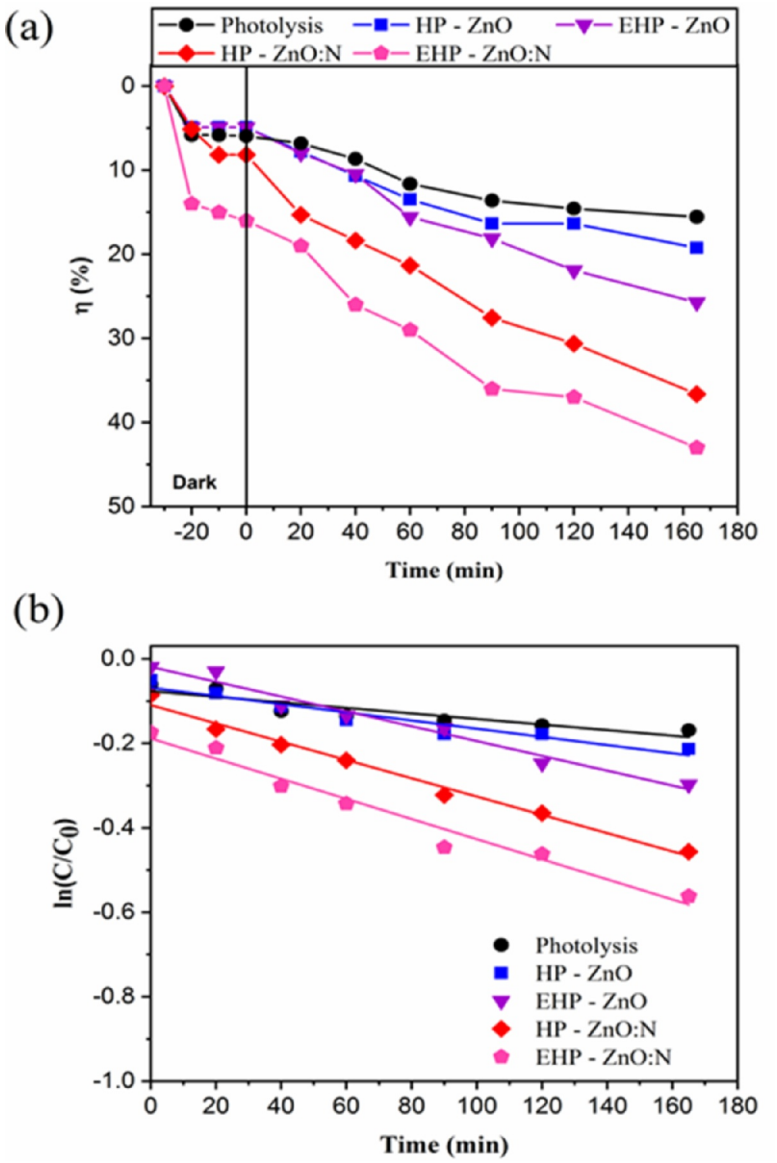

Fig. 9. Photocatalytic study of Rhodamine B dye aqueous solution with C_0 = 1.0 μmol L^{-1} (0.48 mg L^{-1}) under polychromatic irradiation at 25°C. (a) Degradation efficiency by photolysis, heterogeneous photocatalysis (HP) and electrochemically assisted HP (EHP) using ZnO and ZnO:N electrodes and (b) degradation kinetics.

Table 1
Catalytic efficiency and degradation kinetics of Rhodamine B dye in different systems.

Catalytic System	Photocatalyst Film	Catalytic Efficiency (η (%))	Degradation kinetics (k (min^{-1}))
Photolysis		15.6	6.57 × 10^{-4}
HP	ZnO	19.0	9.69 × 10^{-4}
EHP		26.0	17.5 × 10^{-4}
HP	ZnO:N	36.6	21.6 × 10^{-4}
EHP		43.0	23.0 × 10^{-4}

indicated by the XPS results.

The formation of intermediate levels in the prohibited band gap energy, caused by nitrogen doping of ZnO, provides a better electron transport from VB to CB and light absorption as well as a lower recombination rate in ZnO:N film, as observed in photoelectrochemical properties results. Gionco et al. [85] described that the nitrogen-doping process of ZnO provided better photocatalytic activity for solutions containing phenol and 2,4-dichlorophenol, due to variations in sample absorption at different N proportions and the presence of localized states between the prohibited band gap energy. According to theoretical studies by Yu et al. [86], the presence of non-metal atoms such as C and N in the ZnO structure provides the substitution of oxygen atoms due to the similarity between these atoms causing changes in the Fermi level in E_{BG} improving electronic properties and better photocatalytic results.

According to Silva et al [50], the mechanism of RhB photodegradation on ZnO can be described by a cluster model, in which trapping holes are identified as oxygen vacancies (Vo) in oxide disordered structure ($[ZnO_4]^x/[ZnO_3•Vo$). These trapping holes are able to water oxidize to form hydroxyl radical (OH*), which with O_2H* result from O_2 reduction on semiconductor surface by photogenerated electrons, are mostly responsible for RhB degradation [50]. Therefore, the higher ZnO:N film photocatalytic efficiency in relation to ZnO film can also be associated to oxygen vacancies promoted by nitrogen doping on ZnO:N.

4. Conclusion

In this work, ZnO films were successfully obtained by the

electrodeposition method, the calcination temperature study achieved better results for the heated film at 500°C for 1 h and for direct nitrogen doping of ZnO during the electrodeposition process in different N_2 flow rates (10, 20, and 30 $cm^3\ min^{-1}$) heated at 500°C. All prepared films have hexagonal structure (wurtzite) and similar values of direct optical E_{BG} calculated by the Tauc method. Nitrogen doping on ZnO:N film was confirmed by XPS analysis, which indicated that the doping occurred both in an interstitial and substitutional manner. FE-SEM images illustrated a change in the morphology of the ZnO film obtained in the presence of N_2. Photoelectrochemical analyzes indicated that nitrogen-doping with a flow rate of 20 $cm^3\ min^{-1}$ improves electron transport and increases separation of electrons and photogenerated holes, reducting the recombination time of the e^-/h^+ pair. For the analysis of material viability as photocatalyst, oxidative degradation studies of RhB dye in aqueous solution under polychromatic irradiation were tested in the HP and EHP configurations using the ZnO and ZnO:N (20 $cm^3\ min^{-1}$) electrodes as photocatalyst for 165 min. In this study, the photoanodes were biased at +0.7 V vs. Ag/AgCl, and photocatalytic efficiency showed better results because the applied potential caused by suppression of e^-/h^+ pair charge recombination. Thus, the highest photocatalytic activity obtained was for the EHP configuration with the ZnO:N (20 $cm^3\ min^{-1}$) electrode, due to higher stability, lower recombination rate, and better visible radiation absorption caused by the formation of intermediate states in the E_{BG} interval. Hence, the direct doping of ZnO film with nitrogen during the electrodeposition process under N_2 flow proved to be a simple and efficient method of nitrogen doping, with promising potential for doping other semiconductors with nitrogen.

Credit authorship contribution statement

Roberta Y. N. Reis: Conceptualization, Methodology, Formal analysis, Investigation, Data curation, Writing - original draft, Writing - review & editing, Visualization.: Methodology, Investigation. **Aline E. B. Lima**: Resources, Methodology, Investigation, Writing - review & editing. **Maria J. S. Costa:** Investigation, Data curation, Writing - original draft. **João F. Cruz-Filho:** Formal analysis, Investigation, Data curation. **João P. C. Moura**: Formal analysis, Investigation. **Reginaldo S. Santos**: Conceptualization, Writing - review & editing. **Geraldo E. Luz Jr**: Conceptualization, Methodology, Writing - review & editing, Supervision, Project administration.

Declaration of Competing Interest

The authors declare that they have no known competing financial interests or personal relationships that could have appeared to influence the work reported in this paper.

Acknowledgement

This work was funded by the following grants - CNPq (455864/2014-4, 307559/2015-7, 305757/2018-0).

Supplementary materials

Supplementary material associated with this article can be found, in the online version, at doi:10.1016/j.surfin.2020.100675.

References

[1] R. Kant, C. Dwivedi, S. Pathak, V. Dutta, Fabrication of ZnO nanostructures using Al doped ZnO (AZO) templates for application in photoelectrochemical water splitting, Appl. Surf. Sci. 447 (2018) 200, https://doi.org/10.1016/j.apsusc.2018.03.208 112.

[2] S. Hussain, J.R. Steter, S. Gul, A.J. Motheo, Photo-assisted electrochemical degradation of sulfamethoxazole using a Ti/Ru0.3Ti0.7O2 anode: Mechanistic and kinetic features of the process, J. Environ. Manage. 201 (2017) 153–162, https://doi.org/10.1016/j.jenvman.2017.06.043.

[3] V. Sharma, M. Prasad, P. Ilaiyaraja, C. Sudakar, S. Jadkar, Electrodeposition of highly porous ZnO nanostructures with hydrothermal amination for efficient photoelectrochemical activity, Int. J. Hydrogen Energy 44 (2019) 11459–11471, https://doi.org/10.1016/j.ijhydene.2019.03.132.

[4] J. Jiang, Z. Mu, H. Xing, Q. Wu, X. Yue, Y. Lin, Insights into the synergetic effect for enhanced UV/visible-light activated photodegradation activity via Cu-ZnO photocatalyst, Appl. Surf. Sci. 478 (2019) 1037–1045, https://doi.org/10.1016/j.apsusc.2019.02.019.

[5] M. Salem, I. Massoudi, S. Akir, Y. Litaiem, M. Gaidi, K. Khirouni, Photoelectrochemical and opto-electronic properties tuning of ZnO films: Effect of Cu doping content, J. Alloys Compd. 722 (2017) 313–320, https://doi.org/10.1016/j.jallcom.2017.06.113.

[6] R. Qin, F. Meng, M.W. Khan, B. Yu, H. Li, Z. Fan, J. Gong, Fabrication and enhanced photocatalytic property of TiO 2 -ZnO composite photocatalysts, Mater. Lett. 240 (2019) 84–87, https://doi.org/10.1016/j.matlet.2018.12.139.

[7] Y. Mao, Y. Li, Y. Zou, X. Shen, L. Zhu, G. Liao, Solvothermal synthesis and photocatalytic properties of ZnO micro/nanostructures, Ceram. Int. 45 (2019) 1724–1729, https://doi.org/10.1016/j.ceramint.2018.10.054.

[8] C. Ma, W. Jin, X. Duan, X. Ma, H. Han, Z. Zhang, J. Yu, Y. Wu, From the absolute surface energy to the stabilization mechanism of high index polar surface in wurtzite structure: The case of ZnO, J. Alloys Compd. 772 (2019) 482–488, https://doi.org/10.1016/j.jallcom.2018.09.194.

[9] A. Saboor, S.M. Shah, H. Hussain, Band gap tuning and applications of ZnO nanorods in hybrid solar cell: Ag-doped verses Nd-doped ZnO nanorods, Mater. Sci. Semicond. Process. 93 (2019) 215–225, https://doi.org/10.1016/j.mssp.2019.01.009.

[10] M.A.M. Ahmed, W.E. Meyer, J.M. Nel, Structural, optical and electrical properties of the fabricated Schottky diodes based on ZnO, Ce and Sm doped ZnO films prepared via wet chemical technique, Mater. Res. Bull. 115 (2019) 12–18, https://doi.org/10.1016/j.materresbull.2019.03.005.

[11] A. Ievtushenko, O. Khyzhun, V. Karpyna, O. Bykov, V. Tkach, V. Strelchuk, O. Kolomys, S. Rarata, V. Baturin, Karpenko, G. Lashkarev, The effect of Zn3N2 phase decomposition on the properties of highly-doped ZnO: Al, N films, Thin Solid Films 669 (2019) 605–612, https://doi.org/10.1016/j.tsf.2018.11.052.

[12] A. Umar, M.M. Rahman, S.H. Kim, Y.B. Hahn, Zinc oxide nanonail based chemical sensor for hydrazine detection, Chem. Commun. 7345 (2008) 166–168, https://doi.org/10.1039/b711215g.

[13] A. Umar, M.M. Rahman, Y.B. Hahn, ZnO nanorods based hydrazine sensors, J. Nanosci. Nanotechnol. 9 (2009) 4686–4691, https://doi.org/10.1166/jnn.2009.1103.

[14] H. Kim, W. Jae, J. Song, J. Kim, Skein-shaped ZnO/N-doped carbon microstructures as a high performance anode material for lithium-ion batteries, J. Alloys Compd. 772 (2019) 507–515, https://doi.org/10.1016/j.jallcom.2018.09.198.

[15] B.T. Gadisa, S.K. Kassahun, R. Appiah-Ntiamoah, H. Kim, Tuning the charge carrier density and exciton pair separation in electrospun 1D ZnO-C composite nanofibers and its effect on photodegradation of emerging contaminants, J. Colloid Interface Sci. 570 (2020) 251–263, https://doi.org/10.1016/j.jcis.2020.03.002.

[16] M. Faisal, S.B. Khan, M.M. Rahman, A. Jamal, A.M. Asiri, M.M. Abdullah, Synthesis, characterizations, photocatalytic and sensing studies of ZnO nanocapsules, Appl. Surf. Sci. 258 (2011) 672–677, https://doi.org/10.1016/j.apsusc.2011.07.067.

[17] R. Marschall, Semiconductor composites: Strategies for enhancing charge carrier separation to improve photocatalytic activity, Adv. Funct. Mater. 24 (2014) 2421–2440, https://doi.org/10.1002/adfm.201303214.

[18] M.M. Rahman, M.M. Alam, A.M. Asiri, Carbon black co-adsorbed ZnO nanocomposites for selective benzaldehyde sensor development by electrochemical approach for environmental safety, J. Ind. Eng. Chem. 65 (2018) 300–308, https://doi.org/10.1016/j.jiec.2018.04.041.

[19] A.U.R. Bacha, H. Cheng, J. Han, I. Nabi, K. Li, T. Wang, Y. Yang, S. Ajmal, Y. Liu, L. Zhang, Significantly accelerated PEC degradation of organic pollutant with addition of sulfite and mechanism study, Appl. Catal. B 248 (2019) 441–449, https://doi.org/10.1016/j.apcatb.2019.02.049.

[20] B. Dindar, A.C. Güler, Comparison of facile synthesized N doped, B doped and undoped ZnO for the photocatalytic removal of Rhodamine B, Environmental Nanotechnology, Monitor. Manage. 10 (2018) 457–466, https://doi.org/10.1016/j.enmm.2018.09.001.

[21] K. Qi, B. Cheng, J. Yu, W. Ho, Review on the improvement of the photocatalytic and antibacterial activities of ZnO, J. Alloys Compd. 727 (2017) 792–820, https://doi.org/10.1016/j.jallcom.2017.08.142.

[22] N. Salah, A. Hameed, M. Aslam, M.S. Abdel-wahab, S.S. Babkair, F.S. Bahabri, Flow controlled fabrication of N doped ZnO thin films and estimation of their performance for sunlight photocatalytic decontamination of water, Chem. Eng. J. 291 (2016) 115–127, https://doi.org/10.1016/j.cej.2016.01.111.

[23] M. Samadi, M. Zirak, A. Naseri, E. Khorashadizade, A.Z. Moshfegh, Recent progress on doped ZnO nanostructures for visible-light photocatalysis, Thin Solid Films 605 (2016) 2–19, https://doi.org/10.1016/j.tsf.2015.12.064.

[24] C. Bangbai, K. Chongsri, W. Pecharapa, W. Techidheera, Effect of Al and N doping on structural and optical properties of sol-gel derived ZnO thin films, Sains Malaysiana 42 (2013) 239–246, https://doi.org/10.1109/ESciNano.2012.6149675.

[25] P.U. Londhe, N.B. Chaure, Effect of pH on the properties of electrochemically prepared ZnO thin films, Mater. Sci. Semicond. Process. 60 (2017) 5–15, https://doi.org/10.1016/j.mssp.2016.12.005.

[26] P. Gu, X. Wang, T. Li, H. Meng, Investigation of defects in N-doped ZnO powders prepared by a facile solvothermal method and their UV photocatalytic properties, Mater. Res. Bull. 48 (2013) 4699–4703, https://doi.org/10.1016/j.materresbull.2013.08.034.

[27] D. Chakraborty, S. Kaleemulla, N.M. Rao, K. Subbaravamma, G.V. Rao, Structural and optical properties of ITO and Cu doped ITO thin films, AIP Conf. Proc. 1942 (2018) 1–5, https://doi.org/10.1063/1.5029042.

[28] D. Zhang, J. Gong, J. Ma, G. Han, Z. Tong, A facile method for synthesis of N-doped ZnO mesoporous nanospheres and enhanced photocatalytic activity, Dalton Trans. 42 (2013) 16556–16561, https://doi.org/10.1039/c3dt52039k.

[29] W.M. Cho, Y.J. Lin, C.J. Liu, L.R. Chen, Y.T. Shih, P. Chen, Luminescence behavior and compensation effect of N-doped ZnO films deposited by rf magnetron sputtering under various gas-flow ratios of O 2/N2, J. Lumin. 145 (2014) 884–887, https://doi.org/10.1016/j.jlumin.2013.09.029.

[30] Z. Zheng, J. Lin, X. Song, Z. Lin, Optical properties of ZnO nanorod films prepared by CBD method, Chem. Phys. Lett. 712 (2018) 155–159, https://doi.org/10.1016/j.cplett.2018.09.006.

[31] V. Rogé, C. Guignard, G. Lamblin, F. Laporte, I. Fechete, F. Garin, A. Dinia, D. Lenoble, Photocatalytic degradation behavior of multiple xenobiotics using MOCVD synthesized ZnO nanowires, Catal. Today 306 (2018) 215–222, https://doi.org/10.1016/j.cattod.2017.05.088.

[32] J. Wang, E. Elamurugu, N. Franco, E. Alves, A.M. Botelho Do Rego, G. Gonçalves, R. Martins, E. Fortunato, Influence of deposition pressure on N-doped ZnO films by RF magnetron sputtering, J. Nanosci. Nanotechnol. 10 (2010) 2674–2678, https://doi.org/10.1166/jnn.2010.1401.

[33] H. Wu, Z. Hu, B. Li, H. Wang, D. Zhou, X. Zhang, ZnO films grown on ZnO-buffered a-plane sapphire substrates by hydrothermal method, Mater. Lett. 232 (2018) 206–208, https://doi.org/10.1016/j.matlet.2018.08.118.

[34] H. Maleki-Ghaleh, M. Shahzadeh, S.A. Hoseinizadeh, A. Arabi, E. Aghaie, M.H. Siadati, Evaluation of the photo-electro-catalytic behavior of nano-structured ZnO films fabricated by electrodeposition process, Mater. Lett. 169 (2016) 140–143, https://doi.org/10.1016/j.matlet.2016.01.090.

[35] Y. Yang, Y.F. Cheng, One-step facile preparation of ZnO nanorods as high-performance photoanodes for photoelectrochemical cathodic protection, Electrochim. Acta 276 (2018) 311–318, https://doi.org/10.1016/j.electacta.2018.04.206.

[36] C.F. Mah, F.K. Yam, Z. Hassan, Investigation and characterization of ZnO nanostructures synthesized by electrochemical deposition, Procedia Chem. 19 (2016) 83–90, https://doi.org/10.1016/j.proche.2016.03.119.

[37] T. Pauporté, I. Jirka, A method for electrochemical growth of homogeneous nanocrystalline ZnO thin films at room temperature, Electrochim. Acta 54 (2009) 7558–7564, https://doi.org/10.1016/j.electacta.2009.08.022.

[38] J. Tauc, Optical properties and electronic structure of amorphous Ge and Si, Mater. Res. Bull. 3 (1968) 23–46, https://doi.org/10.1016/0025-5408(68)90023-8.

[39] K. Kandpal, J. Singh, N. Gupta, C. Shekhar, Effect of thickness on the properties of ZnO thin films prepared by reactive RF sputtering, J. Mater. Sci. Mater. Electron. 29 (2018) 14501–14507, https://doi.org/10.1007/s10854-018-9584-0.

[40] S. Giménez, J. Bisquert, Photoelectrochemical solar fuel production: From basic principles to advanced devices, Springer, 2016, https://doi.org/10.1007/978-3-319-29641-8.

[41] H.G. Oliveira, L.H. Ferreira, R. Bertazzoli, C. Longo, Remediation of 17-α-ethinylestradiol aqueous solution by photocatalysis and electrochemically-assisted photocatalysis using TiO2 and TiO2/WO3 electrodes irradiated by a solar simulator, Water Res. 72 (2015) 305–314, https://doi.org/10.1016/j.watres.2014.08.042.

[42] R. Beranek, (Photo)electrochemical methods for the determination of the band edge positions of TiO 2-based nanomaterials, Adv. Phys. Chem. 2011 (2011) 80–83, https://doi.org/10.1155/2011/786759.

[43] J. Albertsson, S.C. Abrahams, Kvick, Atomic displacement, anharmonic thermal vibration, expansivity and pyroelectric coefficient thermal dependences in ZnO, Acta Crystallographica Section B 45 (1989) 34–40, https://doi.org/10.1107/S0108768188010109.

[44] T.A. Nirmal Peiris, J.S. Sagu, Y. Hazim Yusof, K.G. Upul Wijayantha, Microwave-assisted low temperature fabrication of ZnO thin film electrodes for solar energy harvesting, Thin Solid Films 590 (2015) 293–298, https://doi.org/10.1016/j.tsf.2015.08.008.

[45] R.B. Corey, R.W.G. Wyckoff, The Crystal Structure of Zinc Hydroxide, Crystalline Mater. 86 (1932) 8–18, https://doi.org/10.1524/zkri.1933.86.1.8.

[46] A.H. Ismail, A.H. Abdullah, Y. Sulaiman, Physical and electrochemical properties of ZnO films fabricated from highly cathodic electrodeposition potentials, Superlattices Microstruct. 103 (2017) 171–179, https://doi.org/10.1016/j.spmi.2017.01.028.

[47] R. Kumari, A. Sahai, N. Goswami, Effect of nitrogen doping on structural and optical properties of ZnO nanoparticles, Prog. Nat. Sci.: Mater. Int. 25 (2015) 300–309, https://doi.org/10.1016/j.pnsc.2015.08.003.

[48] N. Singh, B. Kumari, S. Sharma, S. Chaudhary, S. Upadhyay, V.R. Satsangi, S. Dass, R. Shrivastav, Electrodeposition and sol-gel derived nanocrystalline N-ZnO thin films for photoelectrochemical splitting of water: Exploring the role of microstructure, Renew. Energy 69 (2014) 242–252, https://doi.org/10.1016/j.renene.2014.03.042.

[49] N. Kicir, T. Tüken, O. Erken, C. Gumus, Y. Ufuktepe, Nanostructured ZnO films in forms of rod, plate and flower: Electrodeposition mechanisms and characterization, Appl. Surf. Sci. 377 (2016) 191–199, https://doi.org/10.1016/j.apsusc.2016.03.111.

[50] I.M.P. Silva, G. Byzynski, C. Ribeiro, E. Longo, Different dye degradation mechanisms for ZnO and ZnO doped with N (ZnO:N), J. Mol. Catal. A Chem. 417 (2016) 89–100, https://doi.org/10.1016/j.molcata.2016.02.027.

[51] A.G. Marrani, F. Caprioli, A. Boccia, R. Zanoni, F. Decker, Electrochemically deposited ZnO films: An XPS study on the evolution of their surface hydroxide and defect composition upon thermal annealing, J. Solid State Electrochem. 18 (2014) 505–513, https://doi.org/10.1007/s10008-013-2281-2.

[52] G. Byzynski, C. Melo, D.P. Volanti, M.M. Ferrer, A.F. Gouveia, C. Ribeiro, J. Andrés, E. Longo, The interplay between morphology and photocatalytic activity in ZnO and N-doped ZnO crystals, Mater. Des. 120 (2017) 363–375, https://doi.org/10.1016/j.matdes.2017.02.020.

[53] H. Sudrajat, S. Hartuti, Easily separable N-doped ZnO microspheres with high photocatalytic activity under visible light, Mater. Res. Bull. 102 (2018) 319–323, https://doi.org/10.1016/j.materresbull.2018.02.048.

[54] Z. Wang, Y. Yue, Y. Cao, Preparation and properties of nitrogen doped p-type zinc oxide films by reactive magnetron sputtering, Vacuum 101 (2014) 313–316, https://doi.org/10.1016/j.vacuum.2013.10.001.

[55] A.M. Ferrari-Lima, R.P. De Souza, S.S. Mendes, R.G. Marques, M.L. Gimenes, N.R.C. Fernandes-Machado, Photodegradation of benzene, toluene and xylenes under visible lightapplying N-doped mixed TiO2and ZnO catalysts, Catal. Today 241 (2015) 40–46, https://doi.org/10.1016/j.cattod.2014.03.042.

[56] A. Janotti, C.G. Van De Walle, Fundamentals of zinc oxide as a semiconductor, Rep. Prog. Phys. 72 (2009) 126–501, https://doi.org/10.1088/0034-4885/72/12/126501.

[57] B.M. Rajbongshi, A. Ramchiary, S. Samdarshi, Influence of N-doping on photocatalytic activity of ZnO nanoparticles under visible light irradiation, Mater. Lett. 134 (2014) 111–114, https://doi.org/10.1016/j.matlet.2014.07.073.

[58] Z. Yu, L.C. Yin, Y. Xie, G. Liu, X. Ma, H.M. Cheng, Crystallinity-dependent substitutional nitrogen doping in ZnO and its improved visible light photocatalytic activity, J. Colloid Interface Sci. 400 (2013) 18–23, https://doi.org/10.1016/j.jcis.2013.02.046.

[59] A. Meng, X. Li, X. Wang, Z. Li, Preparation, photocatalytic properties and mechanism of Fe or N-doped Ag/ZnO nanocomposites, Ceram. Int. 40 (2014) 9303–9309, https://doi.org/10.1016/j.ceramint.2014.01.153.

[60] Y.S. Kim, C.H. Park, Rich variety of defects in ZnO via an attractive interaction between O vacancies and Zn interstitials: Origin of n-type doping, Phys. Rev. Lett. 102 (2009) 1–4, https://doi.org/10.1103/PhysRevLett.102.086403.

[61] K.S. Ahn, S.H. Lee, A.C. Dillon, C.E. Tracy, R. Pitts, The effect of thermal annealing on photoelectrochemical responses of WO3 thin films, J. Appl. Phys. 101 (2007) 1–5, https://doi.org/10.1063/1.2729472.

[62] J.A. Oliveira, A.E. Nogueira, M.C.P. Gonçalves, E.C. Paris, C. Ribeiro, G.Y. Poirier, T.R. Giraldi, Photoactivity of N-doped ZnO nanoparticles in oxidative and reductive reactions, Appl. Surf. Sci. 433 (2018) 879–886, https://doi.org/10.1016/j.apsusc.2017.10.110.

[63] K.-S. Ahn, Y. Yan, S.-H. Lee, T. Deutsch, J. Turner, C.E. Tracy, C.L. Perkins, M. Al-Jassim, Photoelectrochemical Properties of N-Incorporated ZnO Films Deposited by Reactive RF Magnetron Sputtering, J. Electrochem. Soc. 154 (2007) B956, https://doi.org/10.1149/1.2754074.

[64] M. Wang, F. Ren, J. Zhou, G. Cai, L. Cai, Y. Hu, D. Wang, Y. Liu, L. Guo, S. Shen, N Doping to ZnO Nanorods for Photoelectrochemical Water Splitting under Visible Light: Engineered Impurity Distribution and Terraced Band Structure, Sci. Rep. 5 (2015) 1–13, https://doi.org/10.1038/srep12925.

[65] S. Allami, Z.D. Abid Ali, Y. Li, H. Hamody, B.H. Jawad, L. Liu, T. Li, Photoelectrochemical performance of N-doped ZnO branched nanowire photoanodes, Heliyon 3 (2017) e00423, https://doi.org/10.1016/j.heliyon.2017.e00423.

[66] V. Tiron, I.L. Velicu, D. Stanescu, H. Magnan, L. Sirghi, High visible light photocatalytic activity of nitrogen-doped ZnO thin films deposited by HiPIMS, Surf. Coat. Technol. 324 (2017) 594–600, https://doi.org/10.1016/j.surfcoat.2016.11.087.

[67] W. He, H.K. Kim, W.G. Wamer, D. Melka, J.H. Callahan, J.J. Yin, Photogenerated charge carriers and reactive oxygen species in ZnO/Au hybrid nanostructures with enhanced photocatalytic and antibacterial activity, J. Am. Chem. Soc. 136 (2014) 750–757, https://doi.org/10.1021/ja410800y.

[68] C. Han, M.Q. Yang, B. Weng, Y.J. Xu, Improving the photocatalytic activity and anti-photocorrosion of semiconductor ZnO by coupling with versatile carbon, PCCP 16 (2014) 16891–16903, https://doi.org/10.1039/c4cp02189d.

[69] M.J.S. Costa, G.S. Costa, A.E.B. Lima, G.E. Luz, E. Longo, L.S. Cavalcante, R.S. Santos, Investigation of charge recombination lifetime in γ-WO3 films modified with Ag0 and Pt0 nanoparticles and its influence on photocurrent density, Ionics 24 (2018) 3291–3297, https://doi.org/10.1007/s11581-018-2640-1.

[70] M. Nischk, P. Mazierski, Z. Wei, K. Siuzdak, N.A. Kouame, E. Kowalska, H. Remita, A. Zaleska-Medynska, Enhanced photocatalytic, electrochemical and photoelectrochemical properties of TiO 2 nanotubes arrays modified with Cu, AgCu and Bi nanoparticles obtained via radiolytic reduction, Appl. Surf. Sci. 387 (2016) 89–102, https://doi.org/10.1016/j.apsusc.2016.06.066.

[71] F. Spadavecchia, S. Ardizzone, G. Cappelletti, L. Falciola, M. Ceotto, D. Lotti, Investigation and optimization of photocurrent transient measurements on nano-TiO2, J. Appl. Electrochem. 43 (2013) 217–225, https://doi.org/10.1007/s10800-012-0485-2.

[72] Z. Ma, O. Linnenberg, A. Rokicinska, P. Kustrowski, A. Slabon, Augmenting the photocurrent of CuWO4 photoanodes by heat treatment in the nitrogen atmosphere, J. Phys. Chem. C 122 (2018) 19281–19288, https://doi.org/10.1021/acs.jpcc.8b02828.

[73] M.A. de Araújo, M.F. Gromboni, F. Marken, S.C. Parker, L.M. Peter, J. Turner, H.C. Aspinall, K. Black, L.H. Mascaro, Contrasting transient photocurrent characteristics for thin films of vacuum-doped “grey” TiO2 and “grey” Nb2O5, Appl. Catal. B 237 (2018) 339–352, https://doi.org/10.1016/j.apcatb.2018.05.065.

[74] A.E.B. Lima, M.J.S. Costa, R.S. Santos, N.C. Batista, L.S. Cavalcante, E. Longo, G.E. Luz, Facile preparation of CuWO4 porous films and their photoelectrochemical properties, Electrochim. Acta 256 (2017) 139–145, https://doi.org/10.1016/j.electacta.2017.10.010.

[75] G. Bhattacharya, K. Jothiramalingam Sankaran, S.B. Srivastava, J.P. Thomas, S. Deshmukh, P. Pobedinskas, S.P. Singh, K.T. Leung, M.K. Van Bael, K. Haenen, S.S. Roy, Probing the flat band potential and effective electronic carrier density in vertically aligned nitrogen doped diamond nanorods via electrochemical method,

Electrochim. Acta 246 (2017) 68–74, https://doi.org/10.1016/j.electacta.2017.06.030.
[76] M.J.S. Costa, G.S. Costa, A.E.B. Lima, G.E.L. Jr., E. Longo, L.S. Cavalcante, R.S. Santos, Photocurrent Response and Progesterone Degradation by Employing WO3 Films Modified with Platinum and Silver Nanoparticles, ChemPlusChem 83 (2018) 1153–1161, https://doi.org/10.1002/cplu.201800534.
[77] X. Chang, M.A. Gondal, A.A. Al-Saadi, M.A. Ali, H. Shen, Q. Zhou, J. Zhang, M. Du, Y. Liu, G. Ji, Photodegradation of Rhodamine B over unexcited semiconductor compounds of BiOCl and BiOBr, J. Colloid Interface Sci. 377 (2012) 291–298, https://doi.org/10.1016/j.jcis.2012.03.021.
[78] D. Yolaçan, N. Demirci Sankir, Enhanced photoelectrochemical and photocatalytic properties of 3D-hierarchical ZnO nanostructures, J. Alloys Compd. 726 (2017) 474–483, https://doi.org/10.1016/j.jallcom.2017.07.314.
[79] B. Bozkurt Çırak, B. Caglar, T. Kılınç, S. Morkoç Karadeniz, Y. Erdoğan, S. Kılıç, E. Kahveci, A. Ercan Ekinci, Ç. Çırak, Synthesis and characterization of ZnO nanorice decorated TiO2 nanotubes for enhanced photocatalytic activity, Mater. Res. Bull. 109 (2019) 160–167, https://doi.org/10.1016/j.materresbull.2018.09.039.
[80] K.V. Kumar, K. Porkodi, F. Rocha, Langmuir-Hinshelwood kinetics - a theoretical study, Catal. Commun. 9 (2008) 82–84., https://doi.org/10.1016/j.catcom.2007.05.019.
[81] A. Samad, S. Ahsan, I. Tateishi, M. Furukawa, H. Katsumata, T. Suzuki, S. Kaneco, Indirect photocatalytic reduction of arsenate to arsenite in aqueous solution with TiO2 in the presence of hole scavengers, Chin. J. Chem. Eng. 26 (2018) 529–533, https://doi.org/10.1016/j.cjche.2017.05.019.
[82] B.S. Wang, R.Y. Li, Z.Y. Zhang, X.L.Wu Xing-Wang, G.A. Cheng, R.T. Zheng, An overlapping ZnO nanowire photoanode for photoelectrochemical water splitting, Catal. Today 321–322 (2019) 100–106, https://doi.org/10.1016/j.cattod.2018.02.028.
[83] R. Ojani, E. Zarei, A new and simple electrochemically assisted photocatalysis sensor of hydrazine using a Ti/TiO2 electrode, J. Braz. Chem. Soc. 24 (2013) 657–662, https://doi.org/10.5935/0103-5053.20130083.
[84] A.B.K. dos Santos, E.M.T. Claro, R.N. Montagnolli, J.M. Cruz, P.R.M. Lopes, E.D. Bidoia, Electrochemically assisted photocatalysis: Highly efficient treatment using thermal titanium oxides doped and non-doped electrodes for water disinfection, J. Environ. Manage. 204 (2017) 255–263, https://doi.org/10.1016/j.jenvman.2017.09.006.
[85] C. Gionco, D. Fabbri, P. Calza, M.C. Paganini, Synthesis, characterization, and photocatalytic tests of N-doped zinc oxide: a new interesting photocatalyst, J. Nanomater. 2016 (2016) 7, https://doi.org/10.1155/2016/4129864.
[86] W. Yu, J. Zhang, T. Peng, New insight into the enhanced photocatalytic activity of N-, C- and S-doped ZnO photocatalysts, Appl. Catal. B 181 (2016) 220–227, https://doi.org/10.1016/j.apcatb.2015.07.031.